Future Batteries 4 (2024) 100012

Contents lists available at ScienceDirect

Future Batteries

journal homepage: www.sciencedirect.com/journal/future-batteries

# Optimized fractional order resonant model of supercapacitors based in error dominant frequency mitigation

K.A. Ottoboni *, P.V.D. da Cruz, R.N. Faria

*Nuclear and Energy Research Institute, Sao Paulo 05508-000, Brazil*

ARTICLE INFO

*Keywords:*
Fractional Order Calculus
Particle swarm optimization
Resonant frequency
Supercapacitor modelling

ABSTRACT

A fractional order model for supercapacitors and a method for obtaining its parameters were proposed based in the association between a simplified model of one integer order capacitor (RC) with a fractional order parallel RLC impedance. Like all parallel RLC impedances, the fractional order parallel RLC impedance has a resonance frequency, however its response depends substantially on the fractional order, making it an important parameter for fitting the model to experimental data. Through the analysis of experimental galvanostatic charge and discharge curve and the application of a heuristic optimization algorithm, the parameters of the proposed model were obtained, pursuing to remove the main frequency component of the error between the data and the RC simplified model. The results demonstrated that the model obtained actually minimized the dominant frequency of the error and also resulted in a decrease in components at other frequencies, highlighting the advantage of the fractional order applied in the RLC proposed model.

## Introduction

Understanding and accurately modeling the behavior of supercapacitors is essential for optimizing their performance and ensuring their reliable integration into various systems, whose security may depend primarily on a sufficiently accurate prediction of the behavior of its components, like the control of complex energy grids. Traditionally, supercapacitor modeling has been primarily approached using conventional differential equation-based methods in the time domain. While these models provide valuable insights into the dynamic behavior of supercapacitors under different operating conditions, they often fail to capture frequency-dependent impedance and nonlinear characteristics, which are crucial for comprehensive analysis and design.

Like presented in [1], a review about the challenge to model the different behaviors of supercapacitors, those models go from simple equivalent circuits to more sophisticated electrochemical models that aim to accurately predict voltage response, charge/discharge dynamics and the impedance variation under various operating conditions.

Fractional order calculus extends the concept of differentiation and integration to non-integer orders and offers a powerful framework for modeling the dynamics of complex systems. For instance, by incorporating fractional order calculus into a device modelling, this can integrate extra information about its characteristics because the fractional order introduces additional degrees of freedom, allowing for more flexibility in shaping a model to the available data.

In recent years, there has been a growing interest from the academic community in studying the possibility of inserting Fractional Order Calculus theories to solve engineering problems, mainly in modeling and control. To exemplify some advances in control: in [2] an optimized cascade control system based on Fractional Order Calculus is proposed, seeking to better deal with disturbance rejection in unstable industrial processes, in [3] and [4] a tri-parametric fractional order controller ($FOI^{\lambda}D^{1-\lambda}$) has shown superior performance in comparison to several contemporary double-loop control schemes in integration-type processes (like continuously stirred tank reactors) which present a non-self-regulating behavior, in [5] and [6] are described fractional augmented control strategies by associating integer and non-integer PID controllers with fractional order filters, in [7] another approach (Fractional Order Lyapunov-Based Model) for the control of continuously stirred tank reactors is presented and in [8] and [9] are presented two distinct approaches, applying fractional order calculus, to optimize the control of "inverted pendulum" type systems. Additionally, in [10] is showed that power quality was improved after considering the fractional order nature of passive components in the modeling and control of a Photovoltaic Inverter System and [11] demonstrates that power-sharing performance was improved after adding an extra degree

* Corresponding author.
*E-mail addresses:* klebberottoboni@alumini.usp.br (K.A. Ottoboni), pedrovitordc@usp.br (P.V.D. da Cruz), rfaria@ipen.br (R.N. Faria).

https://doi.org/10.1016/j.fub.2024.100012
Received 8 September 2024; Received in revised form 3 November 2024; Accepted 15 November 2024
Available online 27 November 2024

of freedom from the implementation of a fractional order derivative droop-control.

Regarding the recent advances in modeling complex systems using fractional-order calculus: In [12] a study is carried out seeking to represent the non-linear characteristics of parallel AC/DC transmission systems from the development of an incommensurate fractional-order model, [13] proposes a fractional calculus-based parameter estimation strategy for a block-oriented Wiener system that aims at increased accuracy with reduced complexity, [14] demonstrates the potential of fractional-order calculus in advancing the modeling and characterization of arterial compliance in human vascular aging and in [15] a new incommensurate order fractional-order neural network model is used as a carrier to design an image encryption scheme.

An important contribution to studies in modeling, analysis and control of fractional-order systems is presented in [16], where the authors present a toolbox (FOMCON), developed for MATLAB environment, intended for fractional-order modeling and control. This toolbox provides easy-to-use, convenient and useful tools for researchers, making it possible to address the particularities of several problems without the time-consuming implementation of basic fractional-order calculus operations, allowing practical results to be obtained quickly.

It is proposed in this work to associate a fractional order parallel RLC impedance in series with a simple RC model, aiming to represent the non-linear characteristics of commercially available supercapacitors. The RC model parameters are going to be obtained directly from the galvanostatic charge/discharge curve and the fractional order RLC will be optimized through a Particle Swarm Optimization Algorithm, in order to minimize the error between the model and experimentally obtained data.

### *Supercapacitor modelling*

The specific properties of supercapacitors, such as: very high-power density, easy maintenance, reliability and durability, in addition to progress in the development of materials and manufacturing processes, have provided a broad growth in their applications in various areas (integration of alternative energy sources, electric vehicles, power quality, embedded electronics, intelligent systems, for example) [1, 17–19]. However, to make the most of its properties, it is necessary to develop models capable of faithfully represent the behavior of the supercapacitor according to the requirements of the system in which it is inserted.

With the aim of improving existing ones and developing new models, the Fractional Order Calculus has been applied in the modeling of supercapacitors [20,21], due to its ability to represent non-linear behavior, such as memory effects, using linear equations.

Several works have developed fractional order models of supercapacitors based in different approaches [1,20]. As presented in [20], one of the bases for constructing fractional order models for supercapacitors, in the frequency domain, is the block called CPE (Fractional Order Constant Phase Element), characterized by the impedance $Z_{CPE} = (1/C_a.s^{\alpha})$. This component is capable of aggregating supercapacitor characteristics such as: Non-Ideal Capacitance, Phase Angle Deviation and Interfacial and Porous Structure Effects. For example, a common model is the CPE in parallel with a resistor, which can represent the overall impedance behavior more accurately than a simple capacitor-resistor model.

In [22] it is introduced the non-integer order model $\alpha = 0.5$ (half order) for supercapacitors, capable of representing their behavior with low computational demand. However, the order of fractional differentiation was fixed in the model, removing the degree of freedom as a benefit from the computational cost caused by fractional order calculation. Some works have applied the method of obtaining a fractional order model for supercapacitors by mimicking the impedance mapping for different frequencies [23–25]. However, this dependence on impedance mapping for different frequencies restricts obtaining results to having a specific experimental apparatus and does not establish a direct relationship with variables of interest to designers that are commonly in the time domain.

Seeking to guide the supercapacitor modeling process towards its response in the time domain: [26] proposed a simplified model based on data obtained from cyclic voltammetry and triangular current sweep chronopotentiometry; [27] proposed a flexible impedance model that adapts to different impedance structures using the time domain charging data when the input is a step voltage and in [28] the supercapacitor equivalent circuit model takes the operating current as the input, the terminal voltage as the output, and the parameters of the fractional equivalent circuit are iteratively estimated by a genetic algorithm. In [29] a time domain analysis is performed in order to obtain an impedance model capable of representing the galvanostatic charge/discharge curves of a supercapacitor, applying a time-dependent capacitance. However, this method means that a nonlinearity is inserted into the model, which makes it difficult to design traditional control systems for plants that consider this model for a supercapacitor.

This work proposes also a time domain analysis, however, maintaining the linearity of the proposed model based in the integration of the CPE (Fractional Order Constant Phase Element) with the priority reduction of the error dominant frequency. The objective of this method is to obtain a fractional order model, in the frequency domain, simpler than those presented in the current literature, from experimental data in the time domain, with an optimized error reduction approach.

### *Fractional Order Calculus – basic definitions*

Fractional Order Calculus is as old as Classical Calculus, however, only after the evolution of computational tools it has been possible to explore the opportunities for applying this mathematical theory. The first important definition is the differential-integral operator $D$, which represents the generalization of the order of integration and differentiation operations from the domain of integer numbers (Classical Calculus) to the domain of real or even complex numbers (Fractional Order Calculus).

The differential-integral operator represents the integration and differentiation in the time-domain, when the orders are defined in the $\mathbb{R}$ domain according to (1). Where $a$ and $t$ are the differential-integral limits, $D$ is the differential-integral operator and $r$ is the arbitrary order in the $\mathbb{R}$ domain as described by [30]. According to (1), the operator $D$ assumes three different functions, i.e., if $r = 0$ the differential-integral operator is equal to the identity, if $r > 0$ the differentiation is selected, otherwise the integration is the function performed.

$$D_t^r = \begin{cases} \dfrac{d^r}{dt^r} & r > 0 \\ 1 & r = 0 \\ \displaystyle\int_a^t (d\tau)^{-r} & r < 0 \end{cases} \tag{1}$$

In [31] is proposed a study describing the fundaments to calculate the differentiation of exponential function (2) with real or complex orders ($r \in \mathbb{R} or r \in \mathbb{C}$). In this solution, $x \in \mathbb{R}$, $c_n$ and $a_n$ are gains also in the $\mathbb{R}$ or $\mathbb{C}$ domains.

$$D^r \sum_{n=0}^{\infty} c_n e^{a_n x} = \sum_{n=0}^{\infty} c_n a_n^r e^{a_n x} \tag{2}$$

The operator $D^r$ in (2) for sine and cosine functions is given by (3) and (4) with $c_n = 1$ and $a_n x = j\omega_x t$. In the sine and cosine functions, $\theta_x = \omega_x t$ is the phase with $\omega_x$ (angular frequency) constant in the $\mathbb{R}$ domain, $j$ is the imaginary term and $t$ is the time-indexer in the $\mathbb{R}$ domain, respectively.

**Table 1**
Pseudo-algorithm of the selected optimization method – Particle Swarm Optimization.

**Pseudo-algorithm for PSO**

**START**
Define the objective function $f(\boldsymbol{x_i})$
For each particle $i = 1 \ldots S$, do:
Initialize the particle positions as a uniformly distributed vector: $\boldsymbol{x} := \boldsymbol{U(b_l, b_s)}$, $\boldsymbol{b_l}$ **and** $\boldsymbol{b_S}$ are the lower and upper limits of the search universe $\boldsymbol{U}$.
Initialize the best positions known as the starting positions: $\boldsymbol{p_i} \leftarrow \boldsymbol{x_i}$
Se $(f(\boldsymbol{p_i}) < (f(\boldsymbol{g}))$ update the best-known position of the swarm: $\boldsymbol{g} \leftarrow \boldsymbol{p_i}$
Initialize particle velocity: $\mathrm{v}_i$
**WHILE** ($t <$ maximum number of iterations)
**FOR** $i = 1 : S$
Choose random numbers $r_p$ e $r_g$ pe belonging to the range [0,1]
Where $j$ is the dimension of particle $i$
**FOR** $j = 1 : n_j$
Update the particle velocity: $\mathrm{v}_{i,j} \leftarrow \omega_{PSO}.\mathrm{v}_{i,j} + \varphi_1.r_p.(p_{i,j} - x_{i,j}) + \varphi_2.r_g.(g_j - x_{i,j})$
Update the particle position: $x_{i,j} = x_{i,j} + \mathrm{v}_{i,j}$
**END FOR**
If $((f(\boldsymbol{x_i}) < (f(\boldsymbol{p_i}))$, update the particle's best-known position: $\boldsymbol{p_i} \leftarrow \boldsymbol{x_i}$
If $(f(\boldsymbol{p_i}) < (f(\boldsymbol{g}))$, update the swarm's best-known position: $\boldsymbol{g} \leftarrow \boldsymbol{p_i}$
**END FOR**
**END WHILE**
Process the results ($g$ represents the best solution found **)**;

Representative pseudo-algorithm of the Particle Swarm Optimization method from [35].

$$D^r\cos(\omega_x t \quad) = {\omega_x}^r \cos\left(\omega_x t \quad - \frac{r\pi}{2}\right) \tag{3}$$

$$D^r\sin(\omega_x t \quad) = {\omega_x}^r \sin\left(\omega_x t \quad - \frac{r\pi}{2}\right) \tag{4}$$

In this type of procedure, the amplitude of $f(t)$ is increased or decreased by ${\omega_x}^r$ according to the order $r \in \mathbb{R}$, while $D^r$ provides a continuous passage between the integration and differentiation producing a displacement of $r\pi/2$ on $f(t)$.

Following the definition presented in (1), i.e. the Fractional Order Calculus core proposal to generalize integration and differentiation operations through the $D^r$ operator, several methods were developed in the literature. In this context, the ones that stand out the most in generalizing these operations for an arbitrary fractional order $r$ are the Grünwald-Letnikov method and the Riemann-Liouville method [30] [32].

In the technique proposed by Grünwald-Letnikov, the differential-integral operator of an arbitrary function $f(t)$ is represented by (5) when the order $r \quad \geq \quad 0$.

$$D_t^r f(t) = \lim_{h\to 0} \frac{1}{h^r} \sum_{k=0}^{[g]} (-1)^k \binom{r}{k} f(t - kh) \tag{5}$$

where,

$$\binom{r}{k} = \frac{\Gamma(r+1)}{\Gamma(k+1)\Gamma(r-k+1)} \tag{6}$$

$$\Gamma(g) = \int_0^\infty e^{-t} t^{g-1} dt \tag{7}$$

and $[g] = \left[\frac{t-a}{h}\right]$ is the integer part of $g$.

This type of procedure is useful because of its simplicity to obtain numerical solutions for fractional order derivatives in differential equations. However, it is necessary to define a minimum value of $h$ (limit of discretization) in the interval $[a,t]$ to obtain real solutions, considering that the computational system has a limit of memory, and (5) depends on the previous values. Therefore, the error associated to (5) can be obtained according to (8), where it is known that $|f(t)| \leq M$ [6], i.e. $M$ is the borders of $f(t)$, and $\varepsilon(t)$ is the error associated to the interval $[a,t]$. Considering sine or cosine functions, $M$ assumes the maximum or minimum values 1 or $-1$ when their amplitudes are equal to 1.

$$\varepsilon(t) \leq \frac{M(t-a)^{-r}}{|\Gamma(1-r)|} \tag{8}$$

The fractional order integrator from Riemann-Liouville is defined by (9), considering $r < 0$.

$${}_aD_t^r f(t) = \frac{1}{\Gamma(-r)} \int_a^t (t-\tau)^{-r-1} f(\tau) d\tau \tag{9}$$

On the other hand, the Riemann-Liouville's definition used in (9) can also be extended for fractional order differential operations (10), when an arbitrary order $r$ satisfies $n - 1 \ < r \leq n$, where $n$ is an integer and $f(t)$ is at least $n$-times differentiable.

**Table 2**
Information from the datasheet of the supercapacitors used to obtain the galvanostatic charge/discharge curves.

| Supercap. | Datasheet Information | |
|---|---|---|
|  | Part Number | SE−5R5-D105VYC3G |
| | Capacitance (F) | 1.0 |
| | $ESR_{max}(\Omega)$ | 22.0 |
| | Manufacturer | *KAMCAP* |
| | Rated Voltage (V) | *5.5* |
|  | Part Number | VEC 2R5 106 MG |
| | Capacitance (F) | 10.0 |
| | $ESR_{max}(m\Omega)$ | 120.0 |
| | Manufacturer | *Vina Tech* |
| | Rated Voltage (V) | *2.5* |

$$ {}_aD_t^r f(t) = \frac{d^n}{dt^n}\left[D_t^{-(n-r)} f(t)\right] $$

$$ = \frac{1}{\Gamma(n-r)}\frac{d^n}{dt^n}\left[\int_a^t \frac{f(\tau)}{(t-\tau)^{r-n+1}} d\tau\right] \quad (10) $$

Additionally, integral-differential operations with fractional order can be approximated in the frequency-domain by transfer functions with integer orders. One of the well-established methodologies is the Refined Oustaloup Recursive Filter (RORF) [30,33]. For an arbitrary fractional order *r*, the approximation for frequencies in the interval $[\omega_b,\ \omega_h]$ can be written as (11), where $2N+2$ is the order of the RORF [33].

$$ s^r \cong \left(\frac{d\omega_h}{b}\right)^r \left(\frac{ds^2 + b\omega_h s}{d(1-r)s^2 + b\omega_h s + dr}\right) \prod_{k_r=}^{N}{}_{-N} \frac{s + \omega'_{k_r}}{s + \omega_{k_r}} \quad (11) $$

where,

$$ \omega'_{k_r} = \left(\frac{d\omega_b}{b}\right)^{\frac{r-2k_r}{2N+1}} \quad (12) $$

$$ \omega_{k_r} = \left(\frac{b\omega_b}{d}\right)^{\frac{r+2k_r}{2N+1}} \quad (13) $$

and $b$ and $d$ are parameters calculated through experimental and theoretical analysis proposed in [33], i.e. $b = 10$ and $d = 9$.

*Particle swarm optimization*

The chosen optimization algorithm, Particle Swarm Optimization (PSO), is an optimization technique based on the behavior of flocks of birds or schools of fish in search of food or escape from predators. It was developed by [34] and its objective was to simulate population dynamics, however, at a certain point in the development, it was observed that the algorithm worked as an optimizer [36]. Table 1 presents a pseudo-algorithm for PSO

Essentially, this algorithm uses the movement of particles $x_i$ through the search universe, each one having its movement speed $v(x_i)$ influenced by its best recorded position $p(x_i)$ and by the position of the particle that presents the best evaluation $g(x_i)$. It was chosen due to its simplicity of implementation and straightforward interpretation of the algorithm adjustment variables ($\omega_{PSO}$, $\varphi_1$ e $\varphi_2$) impact in the optimization process.

## Method description

The data to support the analysis of this work are the galvanostatic charge and discharge curves of two commercially available electrochemical supercapacitors. Table 1 presents the datasheet information of these two capacitors. The first supercapacitor (KAMCAP 1 F 5,5 V) is built by the manufacturer by combining two coin-cells in series. Only one coin-cell was used to obtain the results in galvanostatic charge-discharge measurements. Therefore, the standardized specification for the first supercapacitor is 2 F (one coin) and a maximum operating potential of 2.75 V.

The galvanostatic cycles were carried out using Arbin BT4 equipment with MITSPRO with charge and discharge current of 1 mA for the 2 F supercapacitor and 10 mA for the second 10 F supercapacitor (VinaTech 10 F 2.5 V). These currents were maintained until the electrical potential at the supercapacitor cell terminals reached a value of 1.0 V and 1.1 V for the first and second supercapacitor, respectively ( Table 2).

The inversion of the electric current flux occurs automatically, with the discharge current having its absolute value equal to the value of the charge current, and this condition remains until the moment the electrical potential between the device terminals reaches 0 V, starting a new charge and discharge cycle.

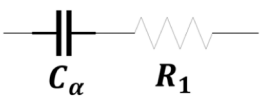


**Fig. 1.** Simple model for the supercapacitor - capacitor in series with a resistance (One capacitor model).

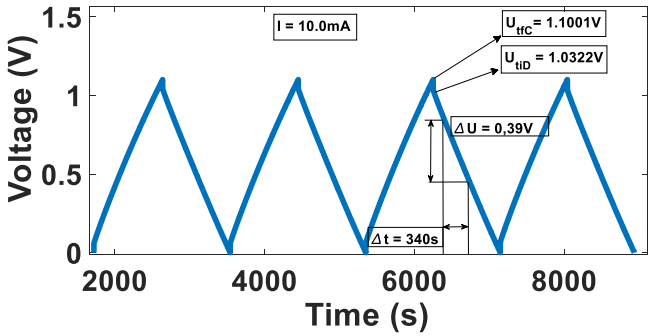


**Fig. 2.** Galvanostatic charge/discharge curve of the 10 F supercapacitor with a current magnitude $I = 10mA$.

*Measured data*

The Fig. 1 presents a simple impedance model for the supercapacitor, bringing its behavior closer to the ideal behavior considering just one capacitor $C_\alpha$ plus a series loss resistance $R_1$. The equivalent series resistance $R_1$, presented in the model of Fig. 1, is obtained through the analysis of the abrupt voltage variation at the point that the current flux is inverted at the galvanostatic charge/discharge cycle and the equivalent capacitance $C_\alpha$ is obtained by the linearization of the discharge curve approximately in the range between 0.8 V and 0,4 V. This method results in the Eq.14 e Eq. 15, respectively.

$$ C_\alpha = \frac{\Delta t \bullet I}{\Delta U} \quad (14) $$

$$ R_1 = \frac{U_{tfC} - U_{tiD}}{2 \bullet I} \quad (15) $$

Where: $I$ is the current absolute value; $\Delta t$ is the time interval associated with the voltage values at which the discharge curve is linearized; $\Delta U$ is the voltage variation between the two points established as limits for linearization, $U_{tfC}$ is the maximum charging voltage value and $U_{tiD}$ is the voltage value at the supercapacitor terminals immediately after the

**Table 3**
Parameters for the One Capacitor Model obtained from the galvanostatic curve (Fig. 2) and Eqs. (14) and (15) – 10 F supercapacitor.

| Model Parameter | One Capacitor Model |
|---|---|
| $C\alpha\ (F)$ | 8,8332 |
| $\alpha$ | 1 |
| $R1(\Omega)$ | 2,9617 |

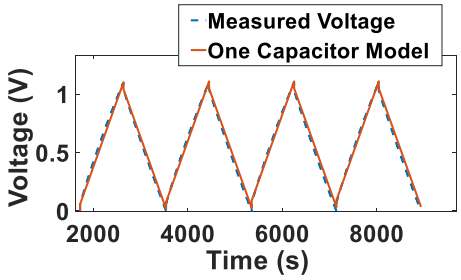


**Fig. 3.** Measured Voltage and voltage obtained in the simulation of the One Capacitor Model for the 10 F supercapacitor.

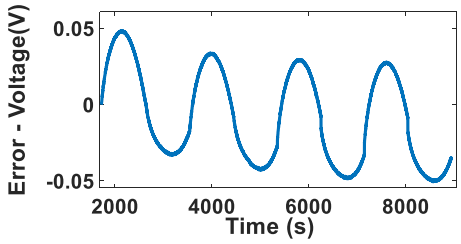


**Fig. 4.** Error between measured data and voltage obtained through the One Capacitor Model for the 10 F supercapacitor.

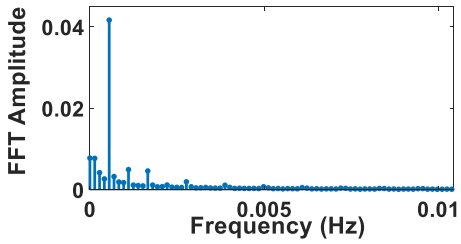


**Fig. 5.** Frequency spectrum of the error of Fig. 3 obtained by Fast-Fourier Transform.

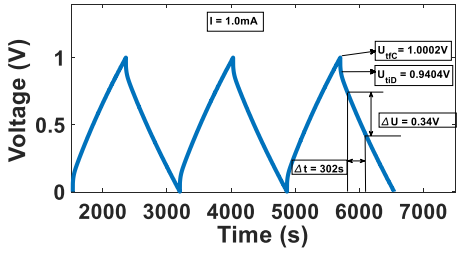


**Fig. 6.** Galvanostatic charge/discharge curve of the 2 F supercapacitor with a current magnitude $I = 1.0mA$.

current flow is reversed.

The Fig. 2 presents the experimental data obtained for the 10 F supercapacitor, with the points used in Eqs. (14) and (15) highlighted,

**Table 4**
Parameters for the One Capacitor Model obtained from the galvanostatic curve (Fig. 6) and Eqs. (14) and (15) – 2 F supercapacitor.

| Model Parameter | One Capacitor Model |
|---|---|
| $C\alpha\ (F)$ | 0,8855 |
| $\alpha$ | 1 |
| $R1(\Omega)$ | 29,8 |

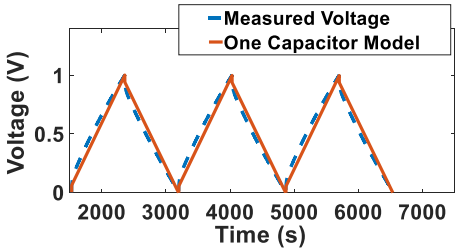


**Fig. 7.** Measured Voltage and voltage obtained in the simulation of the One Capacitor Model for the 2 F supercapacitor.

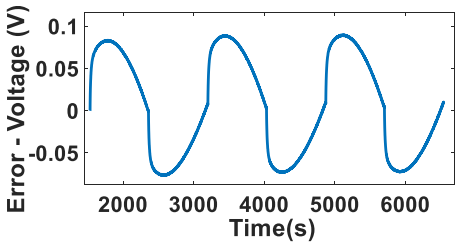


**Fig. 8.** Error between measured data and voltage obtained through the One Capacitor Model for the 2 F supercapacitor.

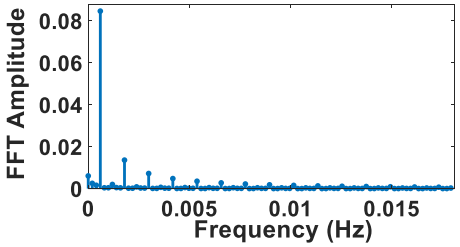


**Fig. 9.** Frequency spectrum of the error of Fig. 8 obtained by Fast-Fourier Transform.

and Table 3 presents the results for the simplified model with just one capacitor. The $\alpha$ suffix is defined as equal to 1.0 and is used to demonstrate that the capacitor considered at this moment is of integer order.

In Fig. 3 is presented a graphical comparison between the measured voltage at the terminals of the 10 F supercapacitor and a simulation applying the parameters from Table 3, and Fig. 4 presents the error between these two curves.

By Fig. 4 is evident the oscillatory characteristic of the error between the experimental data and the simplified model for the 10 F supercapacitor. In Fig. 5 is shown the decomposition of the error in the frequency domain using the Fast Fourier Transform (FFT). The data in Fig. 5 highlights the dominant frequency component in the error.

The same procedure is carried out for the 2 F capacitor. Fig. 6 presents the experimental data collected, highlighting the points applied in (14) and (15) to obtain the parameters from the simplified model for this supercapacitor, which are presented in Table 4.

In a similar way, Fig. 7 presents the graphical comparison between

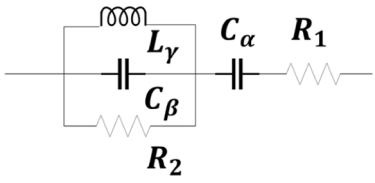


**Fig. 10.** Proposed model for supercapacitor – association of the simple model with a fractional order parallel *RLC* resonant impedance.

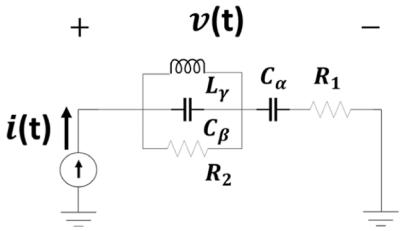


**Fig. 11.** Circuit to obtain the galvanostatic charge/discharge curves with the proposed model for supercapacitors.

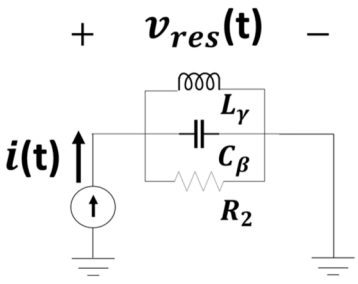


**Fig. 12.** Fractional order parallel RLC circuit from the proposed model.

the experimental data and the model simulation results, and Fig. 8 presents the error between these two curves for the 2 F supercapacitor.

For the 2 F supercapacitor, the error has a larger amplitude when compared to the 10 F and a difference in the shape of the curve, which is expected since, by the graphical comparison of Fig. 7, it is observed a more pronounced non-linear behavior for the 2 F. Fig. 9 presents the frequency spectrum of the error from Fig. 8, and it is evident from the FFT results that the error has significant contributions of multiples of the dominant frequency.

*Proposed model*

The aforementioned oscillatory characteristic of the error for the two supercapacitors leads to the hypothesis that the inclusion of an RLC impedance, designed so that the dominant frequency of the error is nullified, is capable of considerably reduce the error amplitude, and consequently its average value. Therefore, the model proposed in this article is presented in Fig. 10, which is summarized in the insertion of a fractional order parallel RLC impedance in series with the simplified model. Fig. 11 shows the circuit that represents the galvanostatic charge/discharge method with the proposed model, and Eq. (16) shows the fractional order transfer function obtained from this circuit applying the properties of fractional order calculus in the frequency domain [28].

$$\frac{V(s)}{I(s)} = \frac{R_1}{C_\alpha R_1 s^\alpha + 1} + \frac{L_\gamma R_2 s^\gamma}{C_\beta R_2 L_\gamma s^{\beta+\gamma} + L_\gamma s^\gamma + R_2} \tag{16}$$

Where: $s$ is the Laplace Transform variable; $\beta$ is the fractional order of the capacitor $C_\beta$, $\gamma$ is the fractional order of the inductor $L_\gamma$ and $\gamma, \beta, L_\gamma, C_\beta \in \mathbb{R}$.

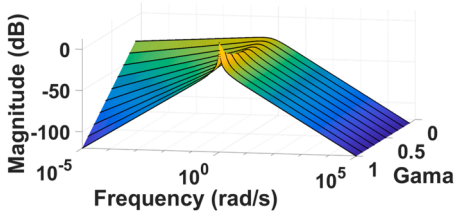


**Fig. 13.** Bode Diagram of the fractional resonant circuit (magnitude in dB) considering $\beta = 1$, $L_\gamma = 100mH$, $C_\beta = 10F$ and $R_2 = 1k\Omega$.

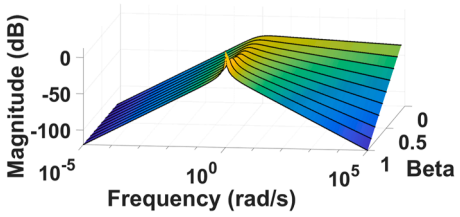


**Fig. 14.** Bode Diagram of the fractional resonant circuit (magnitude in dB) considering $\gamma = 1$, $L_\gamma = 100mH$, $C_\beta = 10F$ and $R_2 = 1k\Omega$.

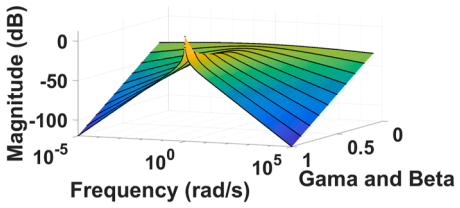


**Fig. 15.** Bode Diagram of the fractional resonant circuit (magnitude in dB) considering $\gamma = \beta$, $L_\gamma = 100mH$, $C_\beta = 10F$ and $R_2 = 1k\Omega$.

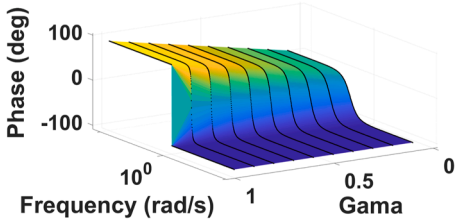


**Fig. 16.** Bode Diagram of the fractional resonant circuit (phase in degrees) considering $\beta = 1$, $L_\gamma = 100mH$, $C_\beta = 10F$ and $R_2 = 1k\Omega$.

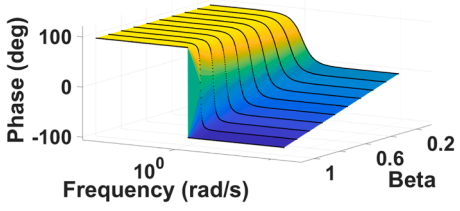


**Fig. 17.** Bode Diagram of the fractional resonant circuit (phase in degrees) considering $\gamma = 1$, $L_\gamma = 100mH$, $C_\beta = 10F$ and $R_2 = 1k\Omega$.

To demonstrate the impact of inserting the fractional variables $\beta$ and $\gamma$ in the transfer function given by (16), the gain and phase variation curves are analyzed, in the frequency domain, considering the variation of these real orders in the interval [0 1]. The FOMCON toolbox developed and described in [16] was used in MATLAB environment to analyze the proposed fractional order transfer function (16). This tool will also

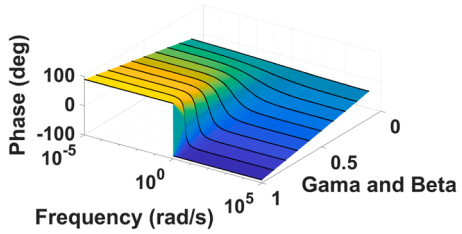


**Fig. 18.** Bode Diagram of the fractional resonant circuit (phase in degrees) considering $\gamma = \beta$, $L_\gamma = 100mH$, $C_\beta = 10F$ and $R_2 = 1k\Omega$.

be used in the PSO optimization algorithm. .

Eq. 12 and Eq. (17) are the RLC circuit representation and the fractional order transfer function from this circuit. Figs. 13 to 15 show the amplitude in *dB* and Figs. 16 to 18 show the phase in degree according to the variation of the frequency, $\beta$ and $\gamma$.

$$\frac{V_{res}(s)}{I(s)} = \frac{L_\gamma R_2 s^\gamma}{C_\beta R_2 L_\gamma s^{\beta+\gamma} + L_\gamma s^\gamma + R_2} = T_{res}(s) \tag{17}$$

To obtain the frequency responses presented in Figs. 13 to 18, the approximation for integer orders is used through the Refined Oustaloup Filter defined in (11), with $N = 3$, and the following values for the passive components: $L_\gamma = 100mH$, $C_\beta = 10F$ and $R_2 = 1k\Omega$, aiming to analyze only the impact of order variation on the transfer function (17) response.

The Fig. 13 demonstrates that the decrease in $\gamma$ order in the interval [0 1] promotes an increase in gain for frequencies below the resonance frequency, transforming the RLC impedance into a low-pass filter. Similarly, decreasing the value of the $\beta$ order (Fig. 14) there is an increase in the gain for frequencies above the resonance frequency, and decreasing these two orders at the same time there is an increase in the frequencies above and below the resonance frequency (Fig. 15).

Similar to the result presented for gain, it shows that there is a linear dependence between the phase variation according to the order variation. By varying only the $\gamma$ order, there is a change in the phase value for frequencies below the resonance frequency (Fig. 16), while by varying the $\beta$ order there is a change only for frequencies above the resonance frequency (Fig. 17). The results presented in Figs. 13 to 18 show that when the fractional orders tend to zero, the inductor and capacitor from the fractional order RLC impedance tend to behave like a resistance, both in terms of gain and phase.

Based on the diagrams from Figs. 13 to 18, the effects of the variation of the fractional order in the RLC parallel impedance were presented. It is clear a direct response in the frequency selectivity of this circuit, demonstrating how it can be configured to respond as a low-pass filter, a high-pass filter or a simple resistance. In addition, it was observed in the phase diagrams that the effect observed in the CPE transfer function [5, 6], of proportional change of the phase according to the variation of the orders, was maintained.

*Optimization – objective function*

Finally, the objective function to be minimized by the PSO optimization algorithm is given by (18). During optimization, each particle $\boldsymbol{x_i} = [\lambda_i]$ generates an objective function $f(\boldsymbol{x_i})$

$$f(\boldsymbol{x_i}) = f_1 + \quad a \bullet f_2 \tag{18}$$

where,

$$f_1(\boldsymbol{x_i}) = \frac{100 \bullet \sqrt{\sum_{t=\ T_s,\ 2T_s,3T_s\ldots}^{t_f} (E(t))^2}}{n} \tag{19}$$

$$f_2(\boldsymbol{x_i}) = \max(|E(t)|) \tag{20}$$

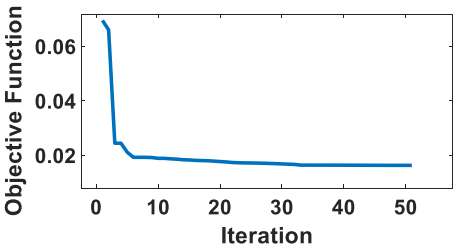


**Fig. 19.** Objective function – PSO 10 F.

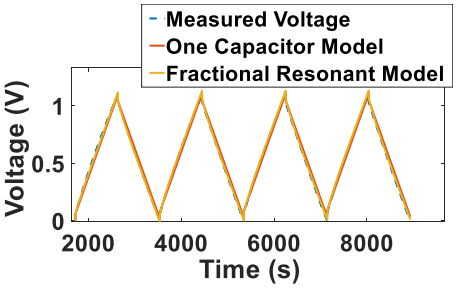


**Fig. 20.** Measured Voltage, voltage obtained from the one capacitor model and from the Fractional RLC model - 10 F supercapacitor.

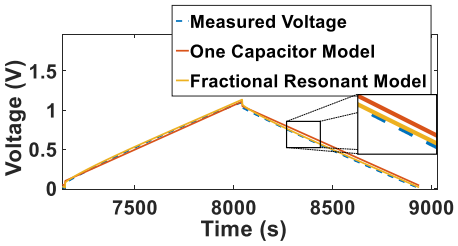


**Fig. 21.** Measured Voltage, voltage obtained from the one capacitor model and from the Fractional RLC model - 10 F supercapacitor (zoom).

$$E(\boldsymbol{t}) = Error_{EX}(t) - lsim(T_{res}(s), i(t)) \tag{21}$$

In (19), $T_S$ is the discretization period of the variable $t$ (time registered in the experimental data) and $t_f$ is the final simulation time, which must correspond to the final time of the experimental data. In (21) the function $Error_{EX}(t)$ is the error presented in Fig. 4 for the 10 F supercapacitor and in Fig. 8 for the 2 F supercapacitor and the function $lsim(T_{res}(s), i(t))$ is the simulation of the response of the transfer function (17) when subjected to the experimentally measured current $i(t)$ as input.

The functions $f_1$ and $f_2$ mean that the objective function $f$ seeks to minimize, respectively, the quadratic error between the voltage value experimentally obtained from the galvanostatic charge/discharge with the result obtained from the transfer function (16). Furthermore, $a$ is a weight (designer adjustment variable) to adjust the influence of each portion of the objective function, here, established as $a = 10$ to scale $f_2$ to values close to $f_1$.

## Results and discussion

The items below present the results obtained after optimizing the parameters of the transfer function defined in (16) from the minimization of the error function. The optimized parameters are: $\gamma$, $\beta$, $L_\gamma$ , $C_\beta$ and $R_2$, and the parameters of the simplified model are the same as those presented in item 2.

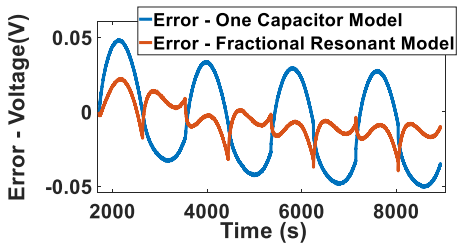


**Fig. 22.** Error between measured data and voltage obtained from the one capacitor model and from the Fractional RLC model - 10 F supercapacitor.

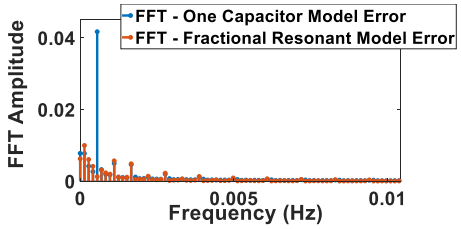


**Fig. 23.** Frequency spectrum of the errors of Fig. 22 obtained by Fast-Fourier Transform.

**Table 5**
Results - proposed model for the 2 F supercapacitor – Particle Swarm Optimization (PSO) Algorithm.

| Model Parameter | One Capacitor Model | Fractional Resonant Model |
|---|---|---|
| $C\alpha\ (F)$ | 8,8332 | 8,8332 |
| $\alpha$ | 1 | 1 |
| $R1(\Omega)$ | 2,9617 | 2,9617 |
| $C\beta\ (F)$ | – | 6,7481 |
| $\beta$ | – | 0,5730 |
| $L\gamma\ (H)$ | – | 116,9495 |
| $\gamma$ | – | 0,5729 |
| $R2\ (k\Omega)$ | – | 13,777 |

*First Supercapacitor – 10 F HyCap*

Figs. 19 to 23 present the results for the 10 F supercapacitor. Fig. 19 shows the values assigned to the objective function at each iteration of the PSO algorithm, demonstrating that there was a rapid convergence, stabilizing after the 30th iteration. Table 5 presents the values obtained for the parameters of the fractional order RLC model.

The data presented in Table 5 allows the following conclusions: for the 10 F capacitor, substantially close values were obtained for $\gamma$ and $\beta$, and, since the error oscillation frequency is low, the values for capacitance and inductance of the RLC model were high. Fig. 20 shows the graphic comparison between the one capacitor model and the fractional order RLC model proposed.

In the Fig. 21, where a zoom of Fig. 20 is shown, it is noticeable that the proposed fractional model gets closer to the values obtained by measurement. However, only in Fig. 22, where the error for the two models is plotted, does the reduction provided by the insertion of the RLC impedance becomes clear.

In order to complement the analysis, Fig. 23 shows the error frequency spectrum for the two models. And, from this result, it is possible to verify the effectiveness of the optimization, since the dominant frequency of the error ($0.55mHz$) was minimized, reducing the amplitude of the dominant frequency by 96.94 % (from 0.04170 to 0.00128) and the mean absolute error by 61.65 % (from 0.0289 to 0.0111).

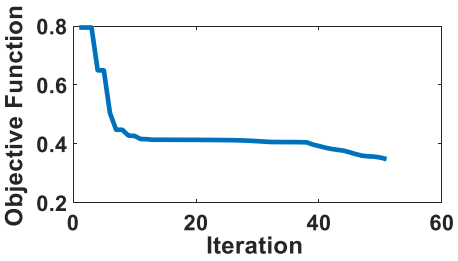


**Fig. 24.** Objective function – PSO 2 F.

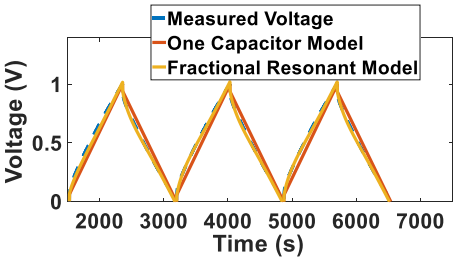


**Fig. 25.** Measured Voltage, voltage obtained from the one capacitor model and from the Fractional RLC model - 2 F supercapacitor.

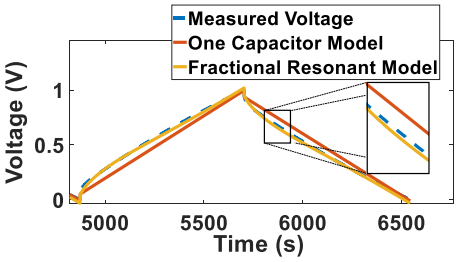


**Fig. 26.** Measured Voltage, voltage obtained from the one capacitor model and from the Fractional RLC model - 2 F supercapacitor (zoom).

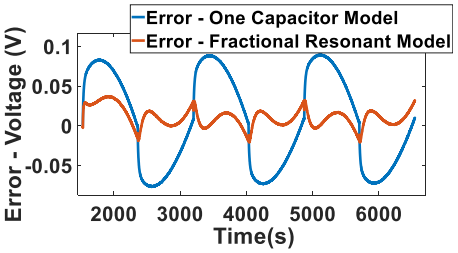


**Fig. 27.** Error between measured data and voltage obtained from the one capacitor model and from the Fractional RLC model - 2 F supercapacitor.

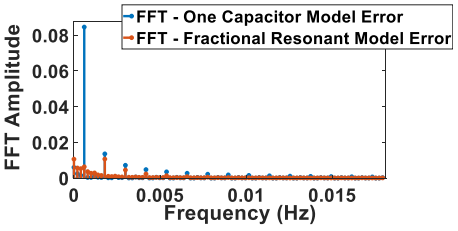


**Fig. 28.** Frequency spectrum of the errors of Fig. 27 obtained by Fast-Fourier Transform.

**Table 6**
Results - proposed model for the 2 F supercapacitor – Particle Swarm Optimization (PSO) Algorithm.

| Model Parameter | One Capacitor Model | Fractional Resonant Model |
|---|---|---|
| $C\alpha\ (F)$ | 0,8855486 | 0,8855486 |
| $\alpha$ | 1 | 1 |
| $R1(\Omega)$ | 29,8 | 29,8 |
| $C\beta\ (F)$ | – | 0,2526 |
| $\beta$ | – | 0, 6001 |
| $L\gamma\ (kH)$ | – | 5,2483 |
| $\gamma$ | – | 0,7491 |
| $R2\ (\Omega)$ | – | 221,332 |

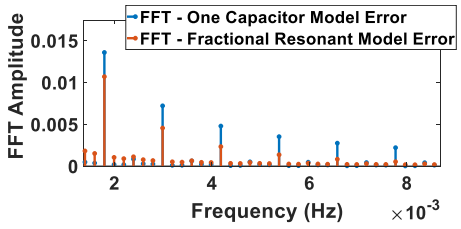


**Fig. 29.** Frequency spectrum of the errors of Fig. 27 obtained by Fast-Fourier Transform (zoom).

*Second supercapacitor – 2 F KAMCAP*

Figs. 24–28 present the results for the 2 F supercapacitor. Fig. 24 shows the values assigned to the objective function at each iteration of the PSO algorithm, demonstrating that there was a convergence, stabilizing after the 45th iteration. Table 6 presents the values obtained for the parameters of the fractional order RLC model.

When analyzing the optimization results presented in Table 6, we see that for the 2 F capacitor the values obtained differ from those obtained for the 10 F capacitor in value and in order of magnitude, for example: for the 2 F capacitor different values were obtained for the $\gamma$ and $\beta$ orders; a value of $5.25kH$ for the inductor and a parallel resistance $R_2$ of $0.2k\Omega$. Fig. 25 shows the graphic comparison between the one capacitor model and the fractional order RLC model proposed for the 2 F capacitor.

In the Fig. 26, where a zoom of Fig. 25 is shown, the improvement in the result is more evident when compared with the results for the 10 F capacitor. Again, Fig. 27, where the error for the two models is plotted, it is clear its reduction for the fractional order RLC model. In order to complement the analysis, Fig. 28 shows the error frequency spectrum for the two models. And, from this result, it is possible to verify the effectiveness of the optimization, since the dominant frequency of the error ($0.60mHz$) was minimized, reducing the amplitude of the dominant frequency by 92.48 % (from 0.08459 to 0.00636) and the mean absolute error by 77.28 % (from 0.0561 to 0.0127).

For this supercapacitor, the effect of the optimization is most notable on multiples of the dominant frequency ($1.8mHz$, $30mHz$, $42mHz$) and the most expressive reduction in the mean absolute error demonstrates this. Fig. 29 shows that effect.

## Conclusion

This study presents a new fractional-order resonant model (RC + fractional order parallel RLC) for supercapacitors, demonstrating superior accuracy compared to simpler integer-order models. Employing experimentally obtained galvanostatic charge-discharge curves and a particle swarm optimization algorithm, the model parameters were optimized to minimize the error, specifically targeting the dominant frequency component. The analysis reveals a significant reduction in the error: a decrease in the dominant frequency amplitude of 96.94 % and in the mean absolute error of 61.65 %, for a 10 F supercapacitor, and a reduction in the dominant frequency amplitude of 92.48 % and the in mean absolute error of 77.28 %, for the 2 F supercapacitor. The last result is particularly notable, indicating the effectiveness of the model in capturing the more pronounced nonlinear behavior observed in the 2 F device. This improved model, characterized by the incorporation of fractional order calculus and its linear structures, provides a more accurate and efficient representation of supercapacitor behavior, particularly advantageous for applications requiring high fidelity modeling, such as control systems applied in power electronics.

## Declaration of Competing Interest

The authors declare that they have no known competing financial interests or personal relationships that could have appeared to influence the work reported in this paper.

## Acknowledgment

The work of K. A. Ottoboni was supported by the Nuclear and Energy Research Institute, São Paulo, Brazil.

## Data Availability

Data will be made available on request.

## References

[1] L. Zhang, H. Xiaosong, W. Zhenpo, S. Fengchun, D.G. Dorrell, Renew. Sustain. Energy Rev. 81 (Part 2) (2018) 1868–1878.
[2] D. Mukherjee, G.L. Raja, P. Kundu, J. Control Autom. Electr. Syst. 32 (2021) 30–41.
[3] P. Aryan, G.L. Raja, U. Mehta, "FOIλD1-λ controller: An alternative to double-loop control schemes for integrating processes," 2023 IEEE 3rd International Conference on Smart Technologies for Power, Energy and Control (STPEC), Bhubaneswar, India, Pages 1–6, 2023.
[4] U. Mehta, P. Aryan, G.L. Raja, IEEE Trans. Circuits Syst. II: Express Briefs 70 (11) (2023) 4166–4170.
[5] S. Dudhe, D.K. Dheer, G.L. Raja, IEEE Trans. Circuits Syst. II: Express Briefs (2024).
[6] D. Mukherjee, G.L. Raja, P. Kundu, A. Ghosh, Asian J. Control 25 (2023) 2165–2182.
[7] D. Mukherjee, G.L. Raja, P. Kundu, A. Ghosh, IFAC-Pap. 55 (1) (2022) 436–441.
[8] O. Saleem, J. Iqbal, IEEE Access 12 (2024) 93185–93196.
[9] D. Mukherjee, G.L. Raja, P. Kundu, et al., Sādhanā 49 (2024) 48.
[10] X. Huang, H. Zhou, W. Huang, Y. Zhang, P. Wang, IEEE Access 12 (2024) 39770–39782.
[11] A.M. AbdelAty, A. Al-Durra, H.H. Zeineldin, S. Kanukollu, E.F. El-Saadany, IEEE Trans. Ind. Inform. 20 (7) (2024) 9427–9444.
[12] Y. Zhang, Y. Lyu, S. Xue, S. Hou, Y. Zi, IEEE Access 12 (2024) 148305–148314.
[13] K. Kothari, IEEE Access 12 (2024) 26281–26294.
[14] M.A. Bahloul, Y. Aboelkassem, Z. Belkhatir, T.-M. Laleg-Kirati, IEEE Open J. Eng. Med. Biol. 5 (2024) 650–660.
[15] Y. Cao, L. Wang, K. Wang, X. Xu, B. Li, IEEE Access 12 (2024) 128179–128186.
[16] A. Tepljakov, E. Petlenkov, J. Belikov, Int. J. Microelectron. Comput. Sci. 2 (2011) 51–62.
[17] B. Wang, C. Wang, Z. Wang, H. Xue, S. Ni, IEEE Trans. Power Electron. 36 (7) (July 2021) 7337–7341.
[18] M. Horn, B. Gupta, J. MacLeod, J. Liu, N. Motta, Curr. Opin. Green. Sustain. Chem. 17 (2019) 42–48.
[19] A. Karimi-Rizvandi, M.B. Sandjareh, M.H. Nazari, M. Ezati-Yaraziz, IEEE Access 9 (2021) 57198–57214.
[20] T.J. Freeborn, B. Maundy, A.S. Elwakil, Mater. Renew. Sustain. Energy 4 (2015).
[21] A. Allagui, A.S. Elwakil, M.E. Fouda, IEEE Trans. Electron Devices 68 (6) (June 2021) 2912–2916.
[22] D. Riu, N. Retière, D. Linzen, Proc. Conf. Rec. 2004 IEEE Ind. Appl. 4 (2004).
[23] Q. Deng, D. Qiu, W. Gu, Y. Chen, B. Zhang, Energy Storage Sci. Technol. 11 (2022) 3371–3380.
[24] G. Maria Lozito, M. Intravaia, F. Corti, G. Patrizi, M. Laschi, L. Ciani, D. Vangi, A. Reatti, IEEE Access 12 (2024) 78449–78462.
[25] V. Martynyuk, M. Ortigueira, Signal Process. 107 (2015) 355–360.
[26] S. Mukhopadhyay, R. Dhaouadi, M. Takrouri, R. Dogga, IEEE Open J. Ind. Electron. Soc. 1 (2020) 166–183.
[27] R. Prasad, K. Kothari, U. Mehta, IEEE Access 7 (2019) 122626–122633.
[28] J. Wang, L. Zhang, J. Mao, J. Zhou, D. Xu, IEEE Access 7 (2019) 52565–52572.
[29] A.P.R. Fernandez, E.A. Périgo, R.N. Faria, J. Energy Storage 51 (2022).
[30] C.A. Monje, Y.Q. Chen, B.M. Vinagre, D. Xue, V. Feliu, Advances in Industrial Control, Springer, 2010.
[31] J. Liouville, J. De. L'École Polytech. 13 (1832) 1–69.
[32] K.S. Miller, B. Ross, Historical Survey, An Introduction to the Fractional Calculus and Fractional Differential Equations, John Wiley & Sons Inc,, 1993.

[33] X. Dingyü, Y.Qua Chen, D.P. Atherton, Fractional-Order Controller – An Introduction. Linear Feedback Control: Analysis and Design with MATLAB, Advances in Design and Control, Society for Industrial and Applied Mathematics,, Philadelphia, 2007.
[34] F. Gabriel, J. Benitez, A. Jorge, B. Peruzzi, R.N. Faria, J. Energy Storage 87 (2024).
[35] R.C. Eberhart, S. Yuhui, Proc. 2001 Congr. Evolut. Comput. 1 (2001) 81–86.
[36] W. Rong-Jong, C. Kun-Lun, L. Jeng-Dao, "Total Sliding-Model-Based Particle Swarm Optimization Control Design For Linear Induction Motor", IEEE Congress on Evolutionary Computation 2007, Pages 4729–4734, 2007.